

Symmetry-Based Tight Binding Modeling of Halide Perovskite Semiconductors

Soline Boyer-Richard, Claudine Katan, Boubacar Traoré, Reinhard Scholz, Jean-Marc Jancu, Jacky Even

▶ **To cite this version:**

Soline Boyer-Richard, Claudine Katan, Boubacar Traoré, Reinhard Scholz, Jean-Marc Jancu, et al.. Symmetry-Based Tight Binding Modeling of Halide Perovskite Semiconductors. Journal of Physical Chemistry Letters, 2016, 7 (19), pp.3833-3840. 10.1021/acs.jpclett.6b01749 . hal-01366310

HAL Id: hal-01366310
https://hal.science/hal-01366310

Submitted on 5 Jan 2017

HAL is a multi-disciplinary open access archive for the deposit and dissemination of scientific research documents, whether they are published or not. The documents may come from teaching and research institutions in France or abroad, or from public or private research centers.

L'archive ouverte pluridisciplinaire **HAL**, est destinée au dépôt et à la diffusion de documents scientifiques de niveau recherche, publiés ou non, émanant des établissements d'enseignement et de recherche français ou étrangers, des laboratoires publics ou privés.

Symmetry-Based Tight Binding Modeling of Halide Perovskite Semiconductors

Soline BOYER-RICHARD[1], Claudine KATAN[2], Boubacar TRAORE[2], Reinhard SCHOLZ[3], Jean-Marc JANCU[1], Jacky EVEN[1*].*

[1]UMR FOTON, CNRS, INSA-Rennes, F-35708 Rennes, France.

[2]Institut des Sciences Chimiques de Rennes, UMR 6226, CNRS, Université de Rennes 1, F-35042 Rennes, France

[3]Dresden Integrated Center for Applied Physics and Photonics Materials, Technische Universität Dresden, Germany

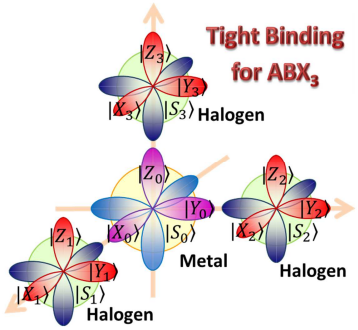
AUTHOR INFORMATION

Corresponding Authors

*soline.richard@insa-rennes.fr *jacky.even@insa-rennes.fr

ABSTRACT Based on a general symmetry analysis, this paper presents an empirical tight-binding (TB) model for the reference Pm-3m perovskite cubic phase of halide perovskites of general formula ABX_3. The TB electronic band diagram, with and without spin orbit coupling effect of $MAPbI_3$ has been determined based on state of the art density functional theory results including many body correction (DFT+GW). It affords access to various properties, including distorted structures, at a significantly reduced computational cost. This is illustrated with the calculation of the band-to-band absorption spectrum, the variation of the band gap under volumetric strain, as well as the Rashba effect for a uniaxial symmetry breaking. Compared to DFT approaches, this empirical model will help to tackle larger issues, such as the electronic band structure of large nanostructures, including many-body effects, or heterostructures relevant to perovskite device modeling suited to the description of atomic-scale features.

TOC GRAPHICS



The potential of 3D Hybrid halide Organic Perovskites (HOP) for photovoltaics has been revealed four years ago.[1–4] Huge progresses have been made to improve the crystalline quality of thin films in solar cell devices, as well as the growth of monocrystalline samples for fundamental studies.[5,6] Many other possible applications of 3D HOP have recently emerged, and layered HOP have gained renewed interest for light emission and are also promising for photovoltaics.[7] 3D HOP can be considered as a new class of semiconductors, with specific optoelectronic properties. To facilitate the analysis and understanding of their properties, some of us have recently proposed to consider the high temperature 3D HOP cubic perovskite phase as a platform to develop a solid-state physics approach.[8–11] It can be exploited within the framework of Density functional theory (DFT), which has now been used extensively for 3D HOP,[9,12–16] but we know from the field of classical IV, III-V or II-VI semiconductors that developing symmetry analyses and empirical Hamiltonians has many advantages. For instance, the one-band or multiband (**k.p**) effective mass approaches close to the band edge,[17,18] have already been used in 3D HOP to investigate various perturbations among which the effect of lattice distortions,[17] the Rashba-Dresselhaus effect,[17,19] the Bethe-Salpeter equation for the simulation of the exciton,[8,11] the radiative lifetime,[20] the selection rules for electron-phonon interactions,[21] and the influence of band gap renormalization, plasma screening and phase space filling on the exciton absorption.[11] These models are close to the free-electron model and built upon the assumption that electrons propagate almost freely with wave functions close to plane waves.

An *alternative* starting point is to use localized atomic orbitals as a basis set to perform band-structure calculations; this is the tight binding (TB) model also known as the linear combination of atomic orbitals (LCAO) approach. It is closer to chemical intuition. This method has been introduced for periodic crystals by Slater and Koster[22] and was extensively used in a wide range

of materials from transition metals to semiconductor crystals.[23] The first description of perovskite crystals using LCAO approach concerns metal oxides[24,25] in the 60's. A detailed description of the LCAO parameterization of perovskite structures was given by Granovskii[26] and takes into account *s*, *p* and *d* type orbitals based on the symmetry analysis by Egorov.[27] Noteworthy, the TB approach is a semi-empirical method that preserves all the symmetry properties of the crystal. However, it is not designed to yield the crystal structure by minimizing the total energy, and an additional (semi-)empirical or DFT-based approach must be used to yield the atomic positions.[28]

Recently, some of us have demonstrated that TB provides an efficient tool for fundamental studies of buried III-V nanostructures with millions atoms,[28] colloidal nanostructures including image charge effects,[29] many-body interactions in semiconductors,[30] and optoelectronic properties of nanostructures including either with direct or indirect band gaps.[31] Besides, state-of-the-art simulations of semiconductor devices, including atomistic effects at the TB level, have also been developed for both inorganic[32–34] and organic semiconductors.[35]

For HOP, Kim and co-workers already proposed a local TB Hamiltonian, developed on an eight functions basis with spin-orbit coupling (SOC).[36] It was designed to model the Rashba effect close to the *R*-point of the perovskite reciprocal lattice and provides clear evidence of sizeable Rashba effect, thus confirming the initial DFT results addressing the importance of spatial and time reversal symmetries in this new family of semiconductors.[17] Unfortunately, the chosen reduced TB scheme was not designed to afford the entire band structure across the whole Brillouin zone (*BZ*). Knudson and coworkers also used an extended Huckel TB model to analyze the effects of band folding in tin-based 2D HOP.[37] Given this background and our preliminary

results,[11] we are convinced that the present work will open up new avenues for understanding HOP devices.

The aim of this article is to build a simple but general TB model for 3D HOP, starting from the symmetry properties of the cubic reference structure of the halide perovskite lattice (Fig. 1a,b), and incorporating their unusual physical properties, like the giant SOC of lead-based HOP. The design of this novel TB model for 3D HOP allows us to illustrate how it can accurately model their properties, using the prototype $MAPbI_3$ compound. Despite the simplicity of the chosen sp^3 model (Fig. 1c), experimental data like effective masses and band gaps are accurately reproduced within this scheme. We further show that absorption coefficient and oscillator strengths can also be deduced from this TB model. Finally, in order to demonstrate the versatility of this approach, we extend the basic cubic perovskite TB model to study the impact of strain, and the Rashba effect related to the loss of inversion symmetry.

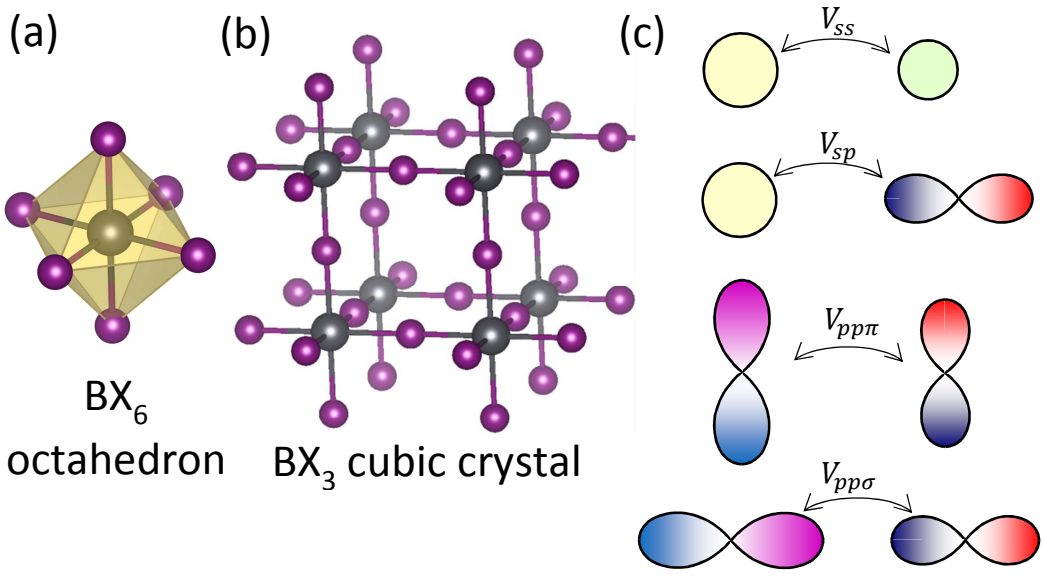


Figure 1. Schematic representation of (a) a single BX_6 octahedron, (b) the BX_3 cubic lattice and (c) *s* and *p* orbitals with the main transfer matrix elements for the sp^3 TB model.

We start by considering the reference cubic structures of the 3D ABX_3 family (Fig. 1b), where A is an organic or inorganic cation located at the center of the unit cell, B is a metal atom (Pb, Sn, …) and X are halogen atoms (X=I, Br, Cl). Obviously, the interpretation of experiments dedicated to electronic and optical properties of HOP as well as their efficient simulation may greatly benefit from symmetry analyses.[8,10] To extensively report on symmetry properties, we herein describe in details the high-temperature 3D perovskite cubic reference phase. But it has been shown that, for example, symmetry breaking is relevant to understand the influence of crystal structure change at a phase transition corresponding to a group-subgroup relationship.[10,17] From a crystallographic point of view, at sufficiently high temperature, 3D HOP have a simple cubic lattice with an octahedron pattern and a central cation. Organic cations automatically break the cubic symmetry, but the cubic space group Pm-3m is restored by dynamical averaging of the cation stochastic reorientations at high temperature. Thus, to perform our symmetry analysis within this TB scheme, only the inorganic atoms of each octahedron are considered (Fig. 1a,b). For each metal atom B and halogen atom X, we consider one *s* and three *p* orbitals (Fig. 1c). No basis functions are considered for any of the A cations, consistently with DFT studies of the electronic states close to the band edges that do not reveal significant weight stemming from A cations.[13]

An isolated octahedron cluster BX_6 belongs to O_h point group symmetry (Fig. 1a), as the cubic crystal ABX_3 (Fig. 1b). However, translational symmetry of crystal modifies orbitals hybridization. For an isolated cluster without SOC, *s* orbitals and *p* orbitals of B atom correspond to A_{1g} and T_{1u} irreducible representation (*IR*), respectively. Meanwhile, *s* and *p* orbitals of the six X atoms correspond to $A_{1g} + E_g + T_{1u}$ and $A_{1g} + E_g + T_{1g} + T_{2g} + 2T_{1u} + T_{2u}$ *IR*, respectively. *s*(B) and *p*(X) orbitals can therefore be hybridized. However, if we consider the

same orbitals of the cubic crystal ABX_3, no hybridization between *s*(B) and *p*(X) is possible at the Γ-point, while it is possible at the *R*-point as illustrated Fig. 2.[10] The aim of the present TB study is to build an empirical model taking into account these specific symmetry considerations, and thus provide accurate simulation of experimental data close to the band gap.

Our TB model is based on ~~a~~ sixteen basis functions without SOC and thirty-two basis functions when taking SOC into account. The symmetries are accounted for under simple and double space groups, respectively.[8,10,13] The crystal pattern contains one B metal atom at $\boldsymbol{r}_0 = (0,0,0)$, and three X halide atoms at $\boldsymbol{r}_1 = \left(\frac{1}{2}, 0,0\right) a$, $\boldsymbol{r}_2 = \left(0, \frac{1}{2}, 0\right) a$ and $\boldsymbol{r}_3 = \left(0,0, \frac{1}{2}\right) a$. The sixteen corresponding atomic orbitals centered at $\boldsymbol{r}_\alpha$ are denoted $|S_\alpha\rangle$ for *s* orbitals and $|X_\alpha\rangle, |Y_\alpha\rangle, |Z_\alpha\rangle$ for *p* orbitals, α = 0 for the B atom and α = 1, 2 or 3 for each of the three halide atoms (see graphical abstract).

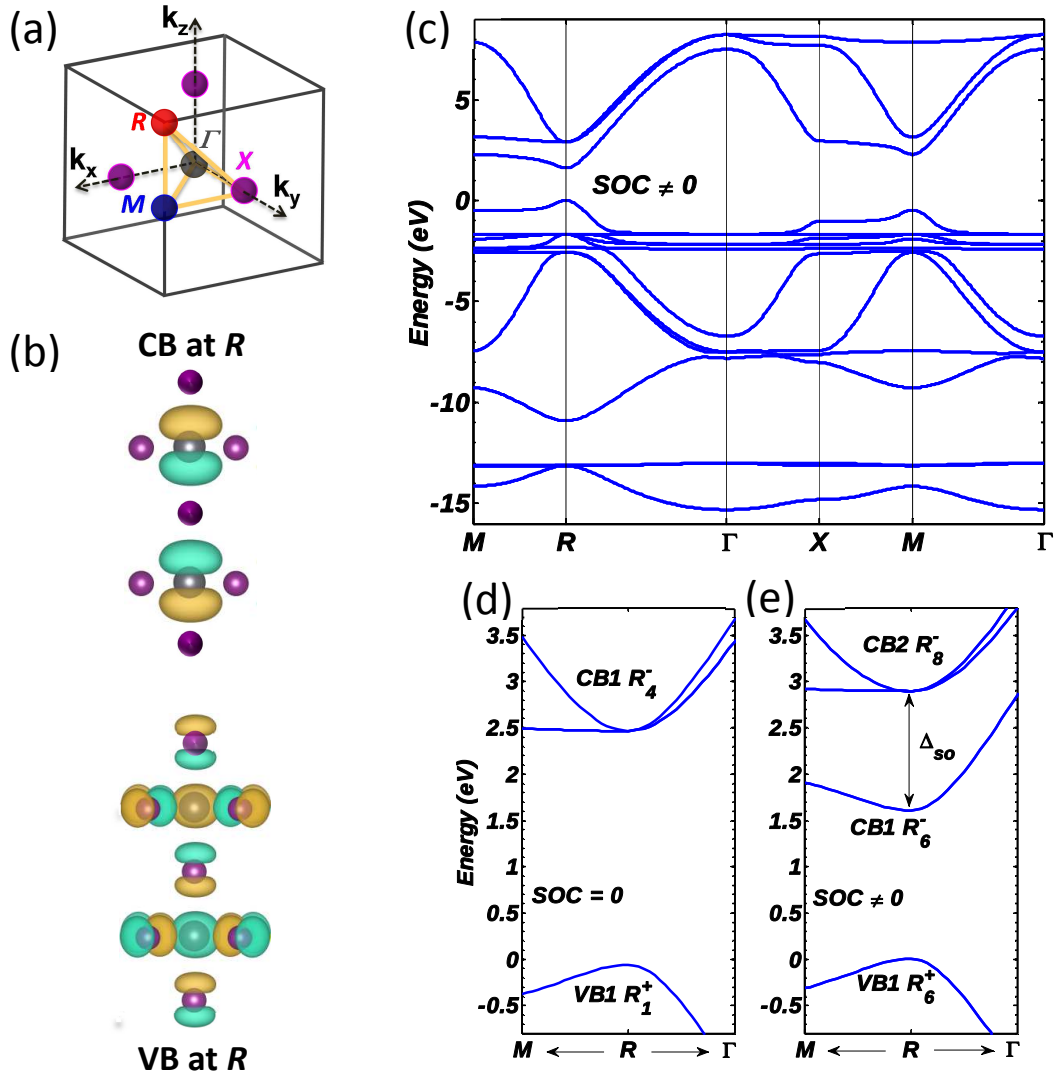


Figure 2. (a) Reciprocal space 3D view showing the first Brillouin Zone (*BZ*) of the Pm3m space group, with high symmetry points. Points denoted *M*, *X* and *R* are zone-boundary points at $\left(\frac{1}{2},\frac{1}{2},0\right)$, $\left(\frac{1}{2},0,0\right)$ and $\left(\frac{1}{2},\frac{1}{2},\frac{1}{2}\right)$ respectively. The *Γ*-point is the *BZ* center. (b) Illustration of the hybridization between *s*(B) and *p*(X) orbitals in the VB (bottom) and between *p*(B) orbitals in the CB (top) at the *R*-point of the *BZ*.[13] (c) Electronic band diagram of $MAPbI_3$ obtained within the TB scheme with SOC, for the Pm-3m pseudo-cubic phase, using parameters of Table 1. The energy of the valence band maximum is set to zero. (d,e) Effect of SOC in the conduction band

close to the *R*-point of the Brillouin zone: SOC lifts the degeneracy of the six conduction bands separating the two lower $J = \frac{1}{2}$ and the 4 upper $J = \frac{3}{2}$ bands. The arrows towards *M* and *Γ* denote the directions in reciprocal space. These zooms correspond to 20% of the *BZ* in each direction. Labels of irreducible representation obtained for simple (d) or double (e) group representation are given at the *R*-point near the band gap.[8,10]

The semi-empirical TB method is a way to solve the Schrödinger equation considering that the crystal Hamiltonian H is the sum between each isolated atom Hamiltonian h_l and a perturbation Hamiltonian H_{int} describing atomic interactions.[38,39] Atomic orbitals $|S_\alpha\rangle, |X_\alpha\rangle, |Y_\alpha\rangle, |Z_\alpha\rangle$ are therefore eigenfunctions of h_l and linear combinations of these atomic orbitals are eigenfunctions of the full crystal Hamiltonian. The coefficients of this linear combination are determined by computing the electronic band structure, which is subsequently compared to data available from experiment and/or first-principles calculations.

Without SOC, nine parameters are considered. This encompasses four different diagonal matrix elements related to the atomic energies of the chemical constituents B and X:

- $E_{s0} = \langle S_0|H|S_0\rangle$
- $E_{p0} = \langle X_0|H|X_0\rangle = \langle Y_0|H|Y_0\rangle = \langle Z_0|H|Z_0\rangle$
- $E_{s1} = \langle S_1|H|S_1\rangle = \langle S_2|H|S_2\rangle = \langle S_3|H|S_3\rangle$
- $E_{p1} = \langle X_\beta|H|X_\beta\rangle = \langle Y_\beta|H|Y_\beta\rangle = \langle Z_\beta|H|Z_\beta\rangle$ where $\beta = 1, 2, 3$ for each X atom.

Five transfer matrix elements refer to the overlap integral of first neighbor atomic functions:

- $V_{ss} = \langle S_0|H_{int}|S_\beta\rangle$ where $\beta = 1, 2, 3$ for each X atom
- $V_{s0p1} = \langle S_0|H_{int}|X_1\rangle = \langle S_0|H_{int}|Y_2\rangle = \langle S_0|H_{int}|Z_3\rangle$
- $V_{p0s1} = \langle X_0|H_{int}|S_1\rangle = \langle Y_0|H_{int}|S_2\rangle = \langle Z_0|H_{int}|S_3\rangle$

- $V_{pp\sigma} = \langle X_0|H_{int}|X_1\rangle = \langle Y_0|H_{int}|Y_2\rangle = \langle Z_0|H_{int}|Z_3\rangle$
- $V_{pp\pi} = \langle Y_0|H_{int}|Y_1\rangle = \langle Y_0|H_{int}|Y_3\rangle = \langle Z_0|H_{int}|Z_1\rangle$ $= \langle Z_0|H_{int}|Z_2\rangle = \langle X_0|H_{int}|X_2\rangle = \langle X_0|H_{int}|X_3\rangle$.

These are schematically represented Fig. 1c. Noteworthy, the overlap integrals between perpendicular *p* orbitals are vanishing. The transfer matrix elements between *s* and *p* orbitals are nonzero if and only if the axis of the *p* orbital contains a *s* orbital center. The complete expression of the 16-band Hamiltonian *H* without SOC is given in the supporting information (SI).

In presence of SOC, the triply degenerate *p* states whose orbital angular momentum is $L = 1$ split into lower $J = \frac{1}{2}$ and upper $J = \frac{3}{2}$ bands, respectively doublet and quartet, whereas SOC is ineffective on *s* states ($L = 0$).[10,13] The 32-band TB Hamiltonian reads: $H_{full} = H + H_{SOC}$.

H_{SOC} is a block-diagonal matrix. For each atom, $\alpha = 0$ for B and $\alpha = 1, 2, 3$ for X, $|X_\alpha \uparrow\rangle, |Y_\alpha \uparrow\rangle, |Z_\alpha \uparrow\rangle$ up spins and $|X_\alpha \downarrow\rangle, |Y_\alpha \downarrow\rangle, |Z_\alpha \downarrow\rangle$ down spin states are coupled by the Pauli matrix H_{SO} written as follows in the basis $\{|X_\alpha \uparrow\rangle, |Y_\alpha \uparrow\rangle, |Z_\alpha \uparrow\rangle, |X_\alpha \downarrow\rangle, |Y_\alpha \downarrow\rangle, |Z_\alpha \downarrow\rangle\}$:

$$H_{SOC} = \frac{\lambda_\alpha}{2}\begin{bmatrix} 0 & -i & 0 & 0 & 0 & 1 \\ i & 0 & 0 & 0 & 0 & -i \\ 0 & 0 & 0 & -1 & i & 0 \\ 0 & 0 & -1 & 0 & i & 0 \\ 0 & 0 & -i & -i & 0 & 0 \\ 1 & i & 0 & 0 & 0 & 0 \end{bmatrix}.$$

Two different SOC values are taken into account: $\Delta_{so0} = \frac{3\lambda_0}{2}$ for *p*(B) orbitals and $\Delta_{so1} = \frac{3\lambda_1}{2} = \frac{3\lambda_2}{2} = \frac{3\lambda_3}{2}$ for *p*(X) orbitals. The 32-band Hamiltonian is larger than the one obtained by Kim et *al.*[36] (*vide supra*) but remains very empty.

To determine the parameters of the TB Hamiltonian relevant to the cubic phase of $MAPbI_3$, we fit the TB band diagram on the following experimental and theoretical data: *(i)* the experimental band gap, $E_G = 1.61\ eV$, as obtained by photoluminescence measurement at room temperature,[40] *(ii)* the reduced effective mass, $\mu = 0.104\ m_0$, as determined by magneto optical measurement,[41] and *(iii)* the band diagram obtained within the quasiparticle self-consistent GW theory (QSGW), with SOC included in the self-consistent cycle.[14] Valence (VB) and/or conduction (CB) band densities of states determined by photoelectron spectroscopy with hard X-rays,[42] ultraviolet and inverse photoemission spectroscopies,[43] as well as pressure study of the band gap,[44] provide further information to assess model parameters. Noteworthy, the complete calculation of the electronic band diagram including SOC presented in this work, takes less than 1 sec on any basic desktop computer without any computational pitfall.

A first set of TB parameters (Table S1, with corresponding computed properties shown Figure S1) allowed to obtain a fit of quite good quality with $E_G = 1.620\ eV$ at the *R*-point (see Brillouin zone sketched Fig. 2a) and a reduced effective mass of $0.116\ m_0$, consistently with the above mentioned experimental results. The SOC value between the predominantly lead-based spin-orbit split-off bands (CB) amounts to $\Delta_{so0} = 1.3\ eV$, in line with the findings of earlier reports.[13,45–47] Noteworthy, this value is consistent with the SOC splitting between *p*-like orbitals reported in atomic energy level tables which amounts to 1.75 eV for lead in its $6s^2 6p$ electronic configuration.[48] Meanwhile, this first set of TB parameters is obtained with $\Delta_{so1} = 1.2\ eV$. This value seems rather high as compared to the 0.94 eV reported for the $5s^2 5p^5$ electronic configuration of iodine.[49]

V_{ss}	V_{s0p1}	V_{p0s1}	$V_{pp\sigma}$	$V_{pp\pi}$	E_{s0}	E_{s1}	E_{p0}	E_{p1}	Δ_{so0}	Δ_{so1}
–1.10	1.19	0.70	–3.65	0.55	–9.01	–13.01	2.34	–1.96	1.30	0.90

Table 1. Tight binding parameters in eV for $MAPbI_3$ band diagram with SOC.

This prompts us to examine the way this parameter influences the computed band diagram. Unfortunately, unlike Δ_{so0} that can be rather easily extracted from the splitting of the doublet and quartet CB (Fig. 2e and S1), Δ_{so1} related to iodine *p*-like states cannot be easily extracted from the highest lying VB, as a consequence of significant hybridization with the lead 6*s* orbitals (Fig. 2b). Thus, we chose $\Delta_{so1} = 0.9\ eV$, close to the value reported in atomic tables, and refine all other TB parameters except $\Delta_{so0} = 1.3\ eV$. Corresponding values and band diagram are given in Table 1 and Fig. 2c, respectively. The band gap remains at the *R*-point with $E_G = 1.603\ eV$. Close to the band gap, effective masses are: $m_h^* = 0.215\ m_0$ for the VB and $m_e^* = 0.218\ m_0$ for the CB, which leads to a reduced effective mass of $0.108\ m_0$, *i.e.* remaining consistent with the experimental value taken as reference.[41]

As a matter of fact, all parameters have to be refined, because the SOC splitting of iodine has a direct impact on the band gap and effective masses, as has been evidenced earlier.[50] This is further illustrated by keeping all parameters fixed expect Δ_{so1}, which is decreased to 0.45 and 0 eV. Corresponding band gaps (reduced effective masses) increase to $E_G = 1.65$ eV (μ = 0.111 m_0) and $E_G = 1.68$ eV (μ = 0.112 m_0), respectively (Figure S2). The comparison of Figure 2c with Figures S1 and S2 clearly evidences that the smaller the splitting Δ_{so1} the smaller the dispersion of the *p*(X) bands lying about 2 to 4 eV below the top of the valence band. For $\Delta_{so1} = 0$, ten of them are totally flat and the quality of the fit with the QSGW significantly deteriorates. We thus proceed with the TB parameters given Table 1 to further investigate the potential of this sp^3 TB model.

Prior to that, we should underline two limitations of the present TB model. They are a direct consequence of the desired simplicity, namely a model simple enough to allow symmetry

consideration to be taken into account close to the band gap. Firstly, the present TB approach is limited to first nearest neighbor interactions and this directly influences the flexibility of the TB model, namely it further contributes to the flatness of some of the band dispersions (vide supra). Secondly, the sharp curvature of VB in the vicinity of 5 eV below the top of the VB (Fig. 2c), much less pronounced in both DFT and QSGW calculations,[8,14] is an indirect consequence of the low hole effective mass that has to be considered to fit both the band edge dispersion and experimental data. However DFT based computations also fail to reproduce the experimental VB density of states in the same energy range.[42,43]

Among others, the optical absorption of a given material is a key parameter for its potential relevance in the field of photovoltaics. The present model allows calculating optical absorption by deriving the TB Hamiltonian. An electromagnetic wave $\vec{A} = \left[A_0 e^{i(\vec{q}\vec{r}-\omega t)} + A_0^* e^{-i(\vec{q}\vec{r}-\omega t)}\right]\vec{e}_{pol}$ creates a perturbation of the Hamiltonian H due to optical excitation $H' = \frac{e}{m_0}\vec{A}\vec{p}$. The photon absorption rate between an initial VB state $|i\rangle$, of energy E_i, and a final CB state $|f\rangle$, of energy E_f, is given by Fermi's golden rule.

$W_{abs} = \frac{2\pi}{\hbar}|\langle f|H'|i\rangle|^2 \delta\left(E_f - E_i - \hbar\omega\right)$ with $\langle f|H'|i\rangle = \frac{eA_0}{m_0}\left\langle f\middle|e^{i\vec{q}\vec{r}}\vec{e}_{pol}.\vec{p}\,\middle|i\right\rangle$

The optical matrix element $M_{i\to f} = \left\langle f\middle|e^{i\vec{q}\vec{r}}\vec{e}_{pol}.\vec{p}\,\middle|i\right\rangle = \left\langle u_{ck}\middle|\vec{e}_{pol}.\vec{p}\,\middle|u_{vk}\right\rangle p_e(k)$ is calculated as $p_e(k) = \frac{m_0}{\hbar}\nabla_k H(k)$, deriving the crystal Hamiltonian for each value of k in the first BZ in the polarization direction $\vec{e}_{pol}$. Left and right side of this bra-ket are eigenstates obtained solving the TB Hamiltonian for each value of k in the *BZ*. To perform the *BZ* integration, the resulting discrete transitions are dressed with a 10 meV Gaussian broadening in order to get smooth spectral functions. Fig. 3a shows the absorption spectrum resulting from this calculation for cubic $MAPbI_3$. The validity of this absorption spectrum extends not further than 3.3eV.

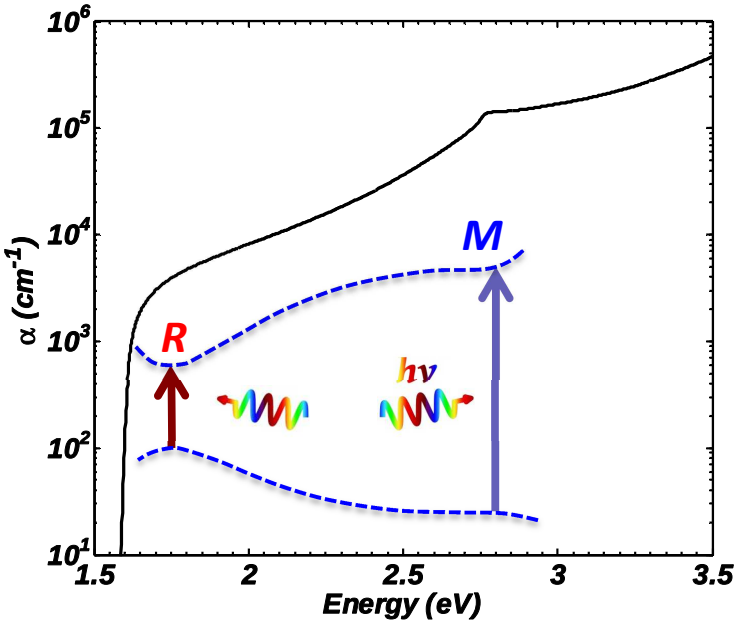


Figure 3. Absorption spectrum (black straight line) of $MAPbI_3$ computed with the sp^3 TB model and parameters given in Table 1. Sketch of VB and CB (blue dashed line) and optical transitions at *R* and *M* points.

The absorption coefficient shows a sharp optical absorption edge, corresponding to the VB1(*R*)-CB1(*R*) optical transition at the *R*-point.[8] It is consistent with experimental data recorded by De Wolf[51] and comparable to the absorption spectrum of GaAs. The calculated absorption slope is modified above 2.75 eV, which corresponds to the VB1(*M*)-CB1(*M*) optical transition at *M*-point and a saddle point in the *R* ➔ *M* direction of the *BZ*.[8,17] The additional absorption feature near 2.75 eV also contains contributions from the VB2(*R*)-CB1(*R*) and VB1(*R*)-CB2(*R*) secondary transitions.[8] This again points the multi-valley and multi-bandgap nature[8] of the optical absorption of HOP leading to high photovoltaic efficiency in very thin layers.

Noteworthy, the shape of the spectrum is similar to that computed by Brivio and co-workers.[14] It might not be surprising, as part of the TB parameterization relies on their calculated band structure. Nonetheless, there is a marked difference for the higher optical feature, which is found above 3 eV in the QSGW spectrum,[14,52] while it is close to the experimental value in the TB spectrum computed with parameters of Table 1, without need of any empirical rescaling. In fact, an empirical rescaling was used for QSGW data, to correctly match the optical spectrum over a large energy range.[52] In addition, when using our first set of TB parameters (Table S1) in which the SOC splitting for iodine atoms is unrealistically high, similar discrepancies with experimental observation are found (Figure S1). Thus, using the TB parameters of Table 1 also improves quantitatively the higher optical features by comparison to state of the art DFT approaches.

General symmetry properties of the halide perovskite lattice,[10] are translated in the TB model to block diagonal Hamiltonians at high symmetry points *Γ*, *R* and *M*. Indeed point groups of vectors $k_R(\frac{1}{2},\frac{1}{2},\frac{1}{2})$ and $k_M\left(\frac{1}{2},\frac{1}{2},0\right)$ are O_h and D_{4h}, respectively. Isotropic optical transitions are predicted because the star of k_R contains only itself whereas the star of k_M contains three arms:[8] $\left(\frac{1}{2},\frac{1}{2},0\right)$, $\left(0,\frac{1}{2},\frac{1}{2}\right)$ and $\left(\frac{1}{2},0,\frac{1}{2}\right)$ which all contribute equally to the observed absorption. The electronic energy eigenfunctions are described as Bloch waves to obtain the effects of point and translational symmetries on the band diagram:

$$\psi_{n,\boldsymbol{k}}(\boldsymbol{r}) = e^{i\boldsymbol{k}\boldsymbol{r}}u_{n,\boldsymbol{k}}(\boldsymbol{r}) \quad (1)$$

where n is the band index, $\boldsymbol{r}$ the position vector and $\boldsymbol{k}$ the wave vector inside the *BZ*. The $e^{i\boldsymbol{k}\boldsymbol{r}}$ phase factor is important to understand the bonding or antibonding character of the wavefunctions.[50]

Here, we propose to associate a basis of symmetrized linear combination of atomic orbitals (SLCAO) used in the TB model to each *IR* obtained by symmetry. We start without SOC. The center of the *BZ* $\Gamma(0,0,0)$ and $R\left(\frac{1}{2},\frac{1}{2},\frac{1}{2}\right)$ are both points where the group of wave vector is O_h, whereas the wave vector at $M\left(\frac{1}{2},\frac{1}{2},0\right)$ belongs to the D_{4h} group, with only sixteen symmetries instead of forty-eight for O_h. In the O_h group, *s* orbitals have $\chi_{phys} = \Gamma_1^+$ or R_1^+ *IR* while *p* orbitals have $\chi_{phys} = \Gamma_4^-$ or R_4^- *IR*.[8,10] In the D_{4h} group, *s* orbitals have $\chi_{phys} = M_1^+$ *IR* while *p* orbitals have $\chi_{phys} = M_2^- + M_5^-$ *IR*.[53] To account for the site symmetry, one determines the site reducible representation χ_{site}. At the Γ-point, the site symmetry correspond to Γ_1^+ for the B atom, and $\Gamma_1^+ + \Gamma_3^+$ for X atoms. The product $\chi_{site} \otimes \chi_{phys}$ provides the *IR* of eigenfunctions. At Γ-point, the SLCAO leads to $\Gamma_1^+, \Gamma_4^-, \Gamma_1^+ + \Gamma_3^+, 2\Gamma_4^- + \Gamma_5^-$ *IR* for *s*(B), *p*(B), *s*(X) and *p*(X) orbitals, respectively, and there is no common *IR* between *s*(B) and *p*(X).[10] At the *R*-point, a similar analysis leads to $R_1^+, R_4^-, R_4^-, R_1^+ + R_3^+ + R_4^+ + R_5^+$ *IR* for the same orbitals. At the *M*-point, this analysis leads to $M_1^+, M_2^- + M_5^-, M_1^+ + M_5^-, M_2^- + M_5^- + M_1^+ + M_2^+ + M_3^+ + M_4^+ + M_5^+$. This decomposition allows determining which orbitals are hybridized at each point of the *BZ* (Table 2).

Point of *BZ*	*s*(B)	*p*(B)	*s*(X)	*p*(X)
R	R_1^+	R_4^-	R_4^-	$R_1^+ + R_3^+ + R_4^+ + R_5^+$
M	M_1^+	$M_2^- + M_5^-$	$M_1^+ + M_5^-$	$M_2^- + M_5^- + M_1^+ + M_2^+ + M_3^+ + M_4^+ + M_5^+$
Γ	Γ_1^+	Γ_4^-;	$\Gamma_1^+ + \Gamma_3^+$	$2\Gamma_4^- + \Gamma_5^-$

Table 2. Irreducible representations (*IR*) of eigenfunctions *within* the TB model at various points of the *BZ* without SOC.

At the *R*-point corresponding to the optical band edge (Fig. 2a, Fig. 3 and Table 2), the symmetry adapted basis functions associated to each *IR* are (without SOC):

- two R_1^+ functions: $|S_0\rangle$, $\frac{1}{\sqrt{3}}(|X_1\rangle + |Y_2\rangle + |Z_3\rangle)$
- two R_3^+ functions: $\frac{1}{\sqrt{6}}(2|Z_3\rangle - |Y_2\rangle - |X_1\rangle)$, $\frac{1}{\sqrt{2}}(|X_1\rangle - |Y_2\rangle)$
- three R_4^+ functions: $\frac{1}{\sqrt{2}}(|Y_1\rangle + |Z_1\rangle)$, $\frac{1}{\sqrt{2}}(|X_2\rangle + |Z_2\rangle)$, $\frac{1}{\sqrt{2}}(|X_3\rangle + |Y_3\rangle)$
- three R_5^+ functions: $\frac{1}{\sqrt{2}}(|Z_1\rangle - |Y_1\rangle)$, $\frac{1}{\sqrt{2}}(|X_2\rangle - |Z_2\rangle)$, $\frac{1}{\sqrt{2}}(|Y_3\rangle - |X_3\rangle)$
- six R_4^- functions: $|X_0\rangle$, $|Y_0\rangle$, $|Z_0\rangle$, $|S_1\rangle$, $|S_2\rangle$, $|S_3\rangle$

This confirms that the totally symmetric R_1^+ correspond to *s*(B) – *p*(X) hybridized atomic orbitals at the top of the VB at point *R*, whereas the bottom of the CB R_4^- correspond to *p*(B) states (Fig. 2b).[10]

In order to account for the influence of the lattice strain, we use a simple variation of the five transfer matrix elements as a function of the interatomic distance d: $V_i = V_{i0}\left(\frac{d_0}{d}\right)^2$ where V_{i0} and d_0 are respectively the transfer matrix element and the lattice parameter, without strain.[38] The band gap variation as a function of the lattice strain, shown Fig. 4, is reversed as compared to classical semiconductors. This is a consequence of the reverse ordering of the CB and VB in halide perovskites.[13] In order to precisely track the origin of the band gap variation, it is possible to calculate analytically the eigenvalues after block diagonalization of the Hamiltonian. The triply degenerate CB minimum ($E_{CB1(R)}, R_4^-(\mathrm{T_{1u}})$) and the VB maximum ($E_{VB1(R)}, R_1^+(\mathrm{A_{1g}})$) correspond respectively to (without SOC):

$$E_{CB1(R)} = \frac{E_{s1} + E_{p0}}{2} + \frac{\sqrt{\left(E_{p0} - E_{s1}\right)^2 + 16{V_{p0s1}}^2}}{2} \qquad R_4^-(\mathrm{T_{1u}})$$

and

$$E_{VB1(R)} = \frac{E_{s0} + E_{p1}}{2} + \frac{\sqrt{(E_{p1} - E_{s0})^2 + 48{V_{s0p1}}^2}}{2} \qquad R\,_1^+(\mathrm{A_{1g}})$$

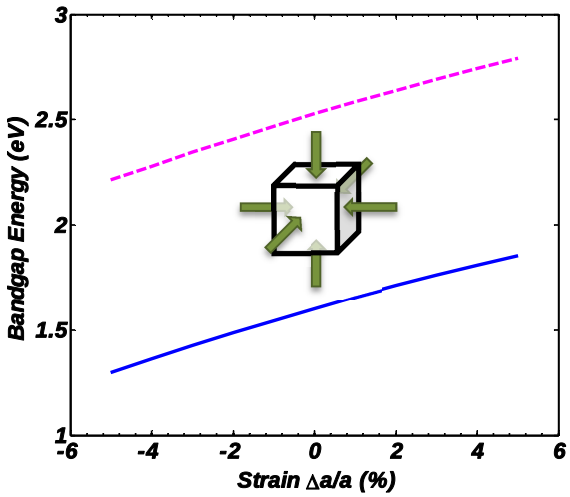


Figure 4. Variation of the band gap as a function of ~~the~~ volumetric strain (sketch in the center), computed with the sp^3 TB model and parameters given in Table 1: with (blue straight line) or without (magenta dashed line) SOC.

For a small variation Δa of the lattice parameter a, the variations of $E_{CB1(R)}$ and $E_{VB1(R)}$ are given by:

$$\delta E_{VB1(R)} \approx \frac{-48{V_{s0p1}}^2}{\sqrt{(E_{p1}-E_{s0})^2+48{V_{s0p1}}^2}} \frac{\Delta a}{a} \tag{2}$$

and

$$\delta E_{CB1(R)} \approx \frac{-16{V_{p0s1}}^2}{\sqrt{(E_{p0}-E_{s1})^2+16{V_{p0s1}}^2}} \frac{\Delta a}{a} \tag{3}$$

This clearly shows that the band gap variation as a function of the strain is related to the transfer integrals between the *s* and *p* orbitals of B and X atoms, V_{s0p1} and V_{p0s1}. The most important variation is related to the VB maximum. The same conclusion was drawn qualitatively

in a recent experimental paper reporting on pressure dependence of the band gap of $MAPbI_3$.[44] Indeed, the authors assumed that the CB has mainly a nonbonding Pb *p* character. It is possible to quantify this aspect with the TB modelling, and state that the *p* orbitals of X atoms and the *s* orbital of the B atom are energetically closer, thus enhancing the coupling (see expressions (2) and (3)). More, V_{s0p1} is significantly larger than V_{p0s1} (Table 1).

With SOC, the CB minimum splits in a double degenerate CB minimum ($E_{CB1(R)}, R\,\bar{6}\,(\mathrm{E_{1/2u}})$) and a quadruple degenerate band lying at higher energy ($E_{CB2(R)}, R\,\bar{8}\,(\mathrm{F_{3/2u}})$):[8]

$$E_{CB1(R)} = \frac{E_{s1} + E_{p0} - 2\Delta_{so0}/3}{2} + \frac{\sqrt{(E_{p0} - E_{s1} - 2\Delta_{so0}/3)^2 + 16{V_{p0s1}}^2}}{2} \qquad R\,\bar{6}\,(\mathrm{E_{1/2u}})$$

and

$$E_{CB2(R)} = \frac{E_{s1} + E_{p0} + \Delta_{so0}/3}{2} + \frac{\sqrt{(E_{p0} - E_{s1} + \Delta_{so0}/3)^2 + 16{V_{p0s1}}^2}}{2} \qquad R\,\bar{8}\,(\mathrm{F_{3/2u}})$$

The variation of E_{CB1} as a function of the strain now reads as follows:

$$\delta E_{CB1(R)} \approx \frac{-16{V_{p0s1}}^2}{\sqrt{(E_{p0} - E_{s1} - 2\Delta_{so0}/3)^2 + 16{V_{p0s1}}^2}} \frac{\Delta a}{a}$$

The additional $\frac{2\Delta_{so0}}{3}$ term at the denominator is much smaller than $E_{p0} - E_{s1}$. This explains why the band gap variation as a function of ~~a~~ volumetric strain, shown Fig. 4, follows the same trend with and without SOC. Moreover, using the experimental value of the bulk modulus reported by Rakita et al.,[54] $K = 14GPa$, the TB band gap decrease computed for a pressure of $32GPa$ is -0.04eV, which compares well with the experimental value of -0.03eV. A refined TB modelling of strain effect is possible by slightly tuning the dependence of the transfer matrix elements as a function of the interatomic distances,[55] but this is beyond the scope of the present paper.

At point $M\left(\frac{1}{2},\frac{1}{2},0\right)$, the basis functions associated to each *IR* read:

- three M_1^+ functions: $|S_0\rangle$, $|S_3\rangle$, $\frac{1}{\sqrt{2}}(|X_1\rangle + |Y_2\rangle)$
- six M_5^- functions: $|X_0\rangle$, $|Y_0\rangle$, $|X_3\rangle$, $|Y_3\rangle$, $|S_1\rangle$, $|S_2\rangle$
- two M_2^- functions: $|Z_0\rangle$, $|Z_3\rangle$
- one M_2^+ function: $\frac{1}{\sqrt{2}}(|Z_1\rangle + |Z_2\rangle)$
- one M_3^+ function: $\frac{1}{\sqrt{2}}(|Z_1\rangle - |Z_2\rangle)$
- one M_4^+ function: $\frac{1}{\sqrt{2}}(|X_1\rangle - |Y_2\rangle)$
- two M_5^+ functions: $|Y_1\rangle$, $|X_2\rangle$

The electronic states at the *M*-point correspond to a saddle point of the Fermi surface,[8] and contribute to an additional feature in the optical absorption spectrum (Fig. 3). The symmetry decomposition of Bloch states at the *M*-point is fully translated in the TB Hamiltonian (See supporting information for the full expression of this Hamiltonian). For example, at point *M*, the TB Hamiltonian is block-diagonal with a 3×3 block for M_1^+, a 6×6 block for M_5^-, a 2×2 block for M_2^- and five diagonal terms for $M_2^+ + M_3^+ + M_4^+ + M_5^+$.

At point *Γ*, the basis functions associated to each *IR* read:

- two Γ_1^+ functions: $|S_0\rangle$, $\frac{1}{\sqrt{3}}(|S_1\rangle + |S_2\rangle + |S_3\rangle)$
- two Γ_3^+ functions: $\frac{1}{\sqrt{3}}(2|S_3\rangle - |S_2\rangle - |S_1\rangle)$, $\frac{1}{\sqrt{2}}(|S_1\rangle - |S_2\rangle)$
- nine Γ_4^- functions: $|X_0\rangle$, $|Y_0\rangle$, $|Z_0\rangle$, $|X_1\rangle$, $|Y_2\rangle$, $|Z_3\rangle$, $\frac{1}{\sqrt{2}}(|Y_1\rangle + |Z_1\rangle)$, $\frac{1}{\sqrt{2}}(|X_2\rangle + |Z_2\rangle)$, $\frac{1}{\sqrt{2}}(|X_3\rangle + |Y_3\rangle)$
- three Γ_5^- functions: $\frac{1}{\sqrt{2}}(|Z_1\rangle - |Y_1\rangle)$, $\frac{1}{\sqrt{2}}(|X_2\rangle - |Z_2\rangle)$, $\frac{1}{\sqrt{2}}(|Y_3\rangle - |X_3\rangle)$

From symmetry consideration, it appears clearly that the *s-p* bonding does not stabilize the VB maximum Γ_1^+ at the *Γ*-point like at the *R*-point; this is a direct consequence of the phase factor in the definition of the Bloch functions (expression (1)).[50]

Finally, in order to illustrate a simple approach of the Rashba effect within a TB model, we shift the position z_3 of the third iodide atom X along the z axis, by a quantity u ($z_3 = \frac{1}{2} + u$) (Fig. 5a). This shift corresponds to a space group change from Pm-3m to P4mm and the creation of a permanent electric dipole along the z axis.[19] Using the variation of the above mentioned transfer matrix elements as a function of interatomic distances, it is straightforward to show that, for small values of u, two phase factors are modified (see supporting information for the definition of h_z, g_z):

$$g_z \longrightarrow (g_z - 4uh_z)e^{-ik_z au}$$

and

$$h_z \longrightarrow (h_z - 4ug_z)e^{-ik_z au}$$

The resulting electronic band diagrams along the $M_X\left(0,\frac{1}{2},\frac{1}{2}\right) - R - M_Y\left(\frac{1}{2},0,\frac{1}{2}\right)$ path of the cubic *BZ* are given in Fig. 5b,c, for a displacement of the axial iodine atom along *Oz* *u*=0.05. Without SOC, the phase transition lifts partially the degeneracy in the CB.[17] Adding SOC lifts totally the degeneracy (Fig. 5c).[17] The Rashba effect is characteristic of a further lifting of the spinor degeneracy in the vicinity of the *R*-point, both in CB and VB, first revealed in the context of HOP in ref. [17] based on DFT calculations. Noteworthy, the band structure along the $R - M_Z$ path does not exhibit such a degeneracy lifting, since the *Oz* polar axis corresponds to the C_4 axis of the structure.[19]

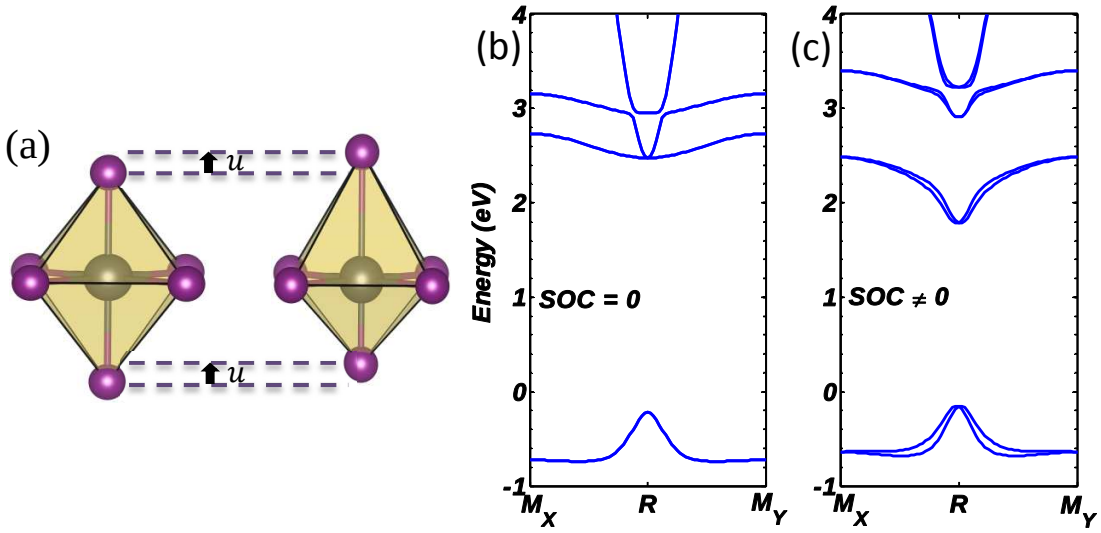


Figure 5. (a) Displacement of the axial iodine atom along the z axis: $z_3 = \frac{1}{2} + u$. This shift corresponds to a space group change from Pm-3m to P4mm. (b) Corresponding electronic band diagram of $MAPbI_3$, along the $M_X - R - M_Y$ path of the cubic *BZ*, obtained within the TB scheme and parameters of Table 1 and $u = 0.05$: (b) without SOC and (c) with SOC.

In summary, based on a symmetry analysis, an semi-empirical TB model for halide perovskites of general formula ABX_3 has been designed and thoroughly investigated for the reference Pm-3m cubic phase. Model parameters have been derived using experimental as well as state-of-the-art DFT data. Particular attention has been paid on the strength and effect of spin-orbit effects, both for the metal and the halogen atoms. $MAPbI_3$ has been considered to illustrate the usefulness and suitability of the model. The calculation of the electronic band diagram is easy and costless as compared to standard DFT calculations. The same holds true for band-to-band absorption spectrum, which is computed from the derivative of the TB Hamiltonian, or to predict the variation of the band gap under volumetric strain. The derived analytic expressions allow

streamlining the findings, *e.g.* providing a natural explanation for the effect of SOC or in terms of orbital hybridization such as *s*-*p* transfer integrals.

The powerfulness of the present TB Hamiltonian is further exemplified with the Rashba effect by considering an uniaxial symmetry breaking. Compared to first-principles approaches, this semi-empirical model challenges us to tackle more difficult questions in terms of size with complex heterostructures, nanostructures or composite materials as well as diversity of physical phenomenon under investigation. We strongly believe that such a TB model, suited for an atomic-scale description, is relevant to perovskite device modeling, as it is for conventional semiconductors.

ASSOCIATED CONTENT

Supporting information available:

- Full expression of tight binding Hamiltonians without SOC
- Simulations with alternative TB parameters.
- Effect of *p*(X) SOC

AUTHOR INFORMATION

Corresponding Authors

*soline.richard@insa-rennes.fr, *jacky.even@insa-rennes.fr

Notes

The authors declare no competing financial interest.

ACKNOWLEDGMENT

This project has received funding from the European Union's Horizon 2020 research and innovation program under the grant agreement No 687008. The information and views set out in this publication are those of the authors and do not necessarily reflect the official opinion of the European Union. Neither the European Union institutions and bodies nor any person acting on their behalf may be held responsible for the use which may be made of the information contained therein. Work at ISCR and FOTON was performed using grant from Cellule Energie du CNRS (SOLHYBTRANS Project) and the University of Rennes 1 (Action Incitative, Défis Scientifiques Emergents 2015).

REFERENCES

(1) Kojima, A.; Teshima, K.; Shirai, Y.; Miyasaka, T. Organometal Halide Perovskites as Visible-Light Sensitizers for Photovoltaic Cells. *J. Am. Chem. Soc.* **2009**, *131*, 6050–6051.

(2) Im, J.-H.; Lee, C.-R.; Lee, J.-W.; Park, S.-W.; Park, N.-G. 6.5% Efficient Perovskite Quantum-Dot-Sensitized Solar Cell. *Nanoscale* **2011**, *3*, 4088.

(3) Lee, M. M.; Teuscher, J.; Miyasaka, T.; Murakami, T. N.; Snaith, H. J. Efficient Hybrid Solar Cells Based on Meso-Superstructured Organometal Halide Perovskites. *Science* **2012**, *338*, 643–647.

(4) Kim, H.-S.; Lee, C.-R.; Im, J.-H.; Lee, K.-B.; Moehl, T.; Marchioro, A.; Moon, S.-J.; Humphry-Baker, R.; Yum, J.-H.; Moser, J. E.; et al. Lead Iodide Perovskite Sensitized All-Solid-State Submicron Thin Film Mesoscopic Solar Cell with Efficiency Exceeding 9%. *Sci. Rep.* **2012**, *2*, 591.

(5) Nie, W.; Tsai, H.; Asadpour, R.; Blancon, J.-C.; Neukirch, A. J.; Gupta, G.; Crochet, J. J.; Chhowalla, M.; Tretiak, S.; Alam, M. A.; et al. High-Efficiency Solution-Processed Perovskite Solar Cells with Millimeter-Scale Grains. *Science* **2015**, *347*, 522–525.

(6) Shi, D.; Adinolfi, V.; Comin, R.; Yuan, M.; Alarousu, E.; Buin, A.; Chen, Y.; Hoogland, S.; Rothenberger, A.; Katsiev, K.; et al. Low Trap-State Density and Long Carrier Diffusion in Organolead Trihalide Perovskite Single Crystals. *Science* **2015**, *347*, 519–522.

(7) Tsai, H.; Nie, W.; Blancon, J.-C.; Stoumpos, C. C.; Asadpour, R.; Harutyunyan, B.; Neukirch, A. J.; Verduzco, R.; Crochet, J. J.; Tretiak, S.; et al. High-Efficiency Two-Dimensional Ruddlesden–Popper Perovskite Solar Cells. *Nature* **2016**, *536*, 312–316.

(8) Even, J.; Pedesseau, L.; Katan, C. Analysis of Multivalley and Multibandgap Absorption and Enhancement of Free Carriers Related to Exciton Screening in Hybrid Perovskites. *J. Phys. Chem. C* **2014**, *118*, 11566–11572.

(9) Even, J.; Pedesseau, L.; Katan, C.; Kepenekian, M.; Lauret, J.-S.; Sapori, D.; Deleporte, E. Solid-State Physics Perspective on Hybrid Perovskite Semiconductors. *J. Phys. Chem. C* **2015**, *119*, 10161–10177.

(10) Even, J. Pedestrian Guide to Symmetry Properties of the Reference Cubic Structure of 3D All-Inorganic and Hybrid Perovskites. *J. Phys. Chem. Lett.* **2015**, *6*, 2238–2242.

(11) Even, J.; Boyer-Richard, S.; Carignano, M.; Pedesseau, L.; Jancu, J.-M.; Katan, C. Theoretical Insights into Hybrid Perovskites for Photovoltaic Applications. *Proc. SPIE* **2016**, *9742*, 97421A.

(12) Mosconi, E.; Amat, A.; Nazeeruddin, M. K.; Grätzel, M.; De Angelis, F. First-Principles Modeling of Mixed Halide Organometal Perovskites for Photovoltaic Applications. *J. Phys. Chem. C* **2013**, *117*, 13902–13913.

(13) Even, J.; Pedesseau, L.; Jancu, J.-M.; Katan, C. Importance of Spin–Orbit Coupling in Hybrid Organic/Inorganic Perovskites for Photovoltaic Applications. *J. Phys. Chem. Lett.* **2013**, *4*, 2999–3005.

(14) Brivio, F.; Butler, K. T.; Walsh, A.; van Schilfgaarde, M. Relativistic Quasiparticle Self-Consistent Electronic Structure of Hybrid Halide Perovskite Photovoltaic Absorbers. *Phys. Rev. B* **2014**, *89*, 155204.

(15) Du, M. H. Efficient Carrier Transport in Halide Perovskites: Theoretical Perspectives. *J. Mater. Chem. A* **2014**, *2*, 9091–9098.

(16) Giorgi, G.; Fujisawa, J.-I.; Segawa, H.; Yamashita, K. Cation Role in Structural and Electronic Properties of 3D Organic–Inorganic Halide Perovskites: A DFT Analysis. *J. Phys. Chem. C* **2014**, *118*, 12176–12183.

(17) Even, J.; Pedesseau, L.; Jancu, J.-M.; Katan, C. DFT and K.p Modelling of the Phase Transitions of Lead and Tin Halide Perovskites for Photovoltaic Cells. *Phys. Status Solidi RRL* **2014**, *8*, 31–35.

(18) Yu, Z. G. Effective-Mass Model and Magneto-Optical Properties in Hybrid Perovskites. *Sci. Rep.* **2016**, *6*, 28576.

(19) Kepenekian, M.; Robles, R.; Katan, C.; Sapori, D.; Pedesseau, L.; Even, J.; Chimiques, S.; Uab, C.; Umr, F. Rashba and Dresselhaus Effects in Hybrid Organic - Inorganic Perovskites: From Basics to Devices. *ACS Nano* **2015**, *9*, 11557–11567.

(20) Fang, H. H.; Raissa, R.; Abdu-Aguye, M.; Adjokatse, S.; Blake, G. R.; Even, J.; Loi, M. A. Photophysics of Organic-Inorganic Hybrid Lead Iodide Perovskite Single Crystals. *Adv. Funct. Mater.* **2015**, *25*, 2378–2385.

(21) Nie, W.; Blancon, J.-C.; Neukirch, A. J.; Appavoo, K.; Tsai, H.; Chhowalla, M.; Alam, M. A.; Sfeir, M. Y.; Katan, C.; Even, J.; et al. Light-Activated Photocurrent Degradation and Self-Healing in Perovskite Solar Cells. *Nat. Commun.* **2016**, *7*, 11574.

(22) Slater, J. C.; Koster, G. F. Simplified LCAO Method for the Periodic Potential Problems. *Phys. Rev.* **1954**, *94*, 1498–1524.

(23) Jancu, J.; Scholz, R.; Beltram, F.; Bassani, F. Empirical Spds * Tight-Binding Calculation for Cubic Semiconductors : General Method and Material Parameters. *Phys. Rev. B* **1998**, *57*, 6493.

(24) Kahn, A. H.; Leyendecker, A. J. Electronic Energy Bands in Strontium Tintanate. *Phys. Rev.* **1964**, *135*, 447–450.

(25) Honig, J. M.; Dimmock, J. O.; Kleiner, W. H. ReO3 Band Structure in the Tight-Binding Approximation. *J. Chem. Phys.* **1969**, *50*, 5232–5242.

(26) Granovskii, V. G.; Sindeev, Y. G. Formulas of the Tight-Binding Interpolation Method for Crystals of Perovskite Type. *Sov. Phys. J.* **1975**, *16*, 164–166.

(27) Egorov, R. F.; Reser, B. I.; Shirokovskii, V. P. Consistent Treatment of Symmetry in the Tight Binding Approximation. *Phys. Status Solidi* **1968**, *26*, 391–408.

(28) Robert, C.; Cornet, C.; Turban, P.; Nguyen Thanh, T.; Nestoklon, M. O.; Even, J.; Jancu, J. M.; Perrin, M.; Folliot, H.; Rohel, T.; et al. Electronic, Optical, and Structural Properties of (In,Ga)As/GaP Quantum Dots. *Phys. Rev. B* **2012**, *86*, 205316.

(29) Benchamekh, R.; Gippius, N. a.; Even, J.; Nestoklon, M. O.; Jancu, J.-M.; Ithurria, S.; Dubertret, B.; Efros, A. L.; Voisin, P. Tight-Binding Calculations of Image-Charge Effects in Colloidal Nanoscale Platelets of CdSe. *Phys. Rev. B* **2014**, *89*, 35307.

(30) Benchamekh, R.; Raouafi, F.; Even, J.; Ben Cheikh Larbi, F.; Voisin, P.; Jancu, J.-M. Microscopic Electronic Wave Function and Interactions between Quasiparticles in Empirical Tight-Binding Theory. *Phys. Rev. B* **2015**, *91*, 45118.

(31) Robert, C.; Pereira Da Silva, K.; Nestoklon, M. O.; Alonso, M. I.; Turban, P.; Jancu, J.-M.; Even, J.; Carrère, H.; Balocchi, A.; Koenraad, P. M.; et al. Electronic Wave Functions and Optical Transitions in (In,Ga)As/GaP Quantum Dots. *Phys. Rev. B* **2016**, *94*, 75445.

(32) Klimeck, G.; Ahmed, S. S.; Hansang Bae; Kharche, N.; Clark, S.; Haley, B.; Sunhee Lee; Naumov, M.; Hoon Ryu; Saied, F.; et al. Atomistic Simulation of Realistically Sized Nanodevices Using NEMO 3-D -Part I: Models and Benchmarks. *IEEE Trans. Electron Devices* **2007**, *54*, 2079–2089.

(33) Klimeck, G.; Ahmed, S. S.; Kharche, N.; Korkusinski, M.; Usman, M.; Prada, M.; Boykin, T. B. Atomistic Simulation of Realistically Sized Nanodevices Using NEMO 3-D - Part II: Applications. *IEEE Trans. Electron Devices* **2007**, *54*, 2090–2099.

(34) Auf der Maur, M.; Galler, B.; Pietzonka, I.; Strassburg, M.; Lugauer, H.; Di Carlo, A. Trap-Assisted Tunneling in InGaN/GaN Single-Quantum-Well Light-Emitting Diodes. *Appl. Phys. Lett.* **2014**, *105*, 133504.

(35) Fallahpour, A. H.; Gagliardi, A.; Santoni, F.; Gentilini, D.; Zampetti, A.; Auf der Maur, M.; Di Carlo, A. Modeling and Simulation of Energetically Disordered Organic Solar Cells. *J. Appl. Phys.* **2014**, *116*, 184502.

(36) Kim, M.; Im, J.; Freeman, a. J.; Ihm, J.; Jin, H. Switchable S = 1/2 and J = 1/2 Rashba Bands in Ferroelectric Halide Perovskites. *Proc. Natl. Acad. Sci.* **2014**, *111*, 6900–6904.

(37) Knutson, J. L.; Martin, J. D.; Mitzi, D. B. Tuning the Band Gap in Hybrid Tin Iodide Perovskite Semiconductors Using Structural Templating. *Inorg. Chem.* **2005**, *44*, 4699–4705.

(38) Yu, P. Y.; Cardona, M. *Fundamentals of Semiconductors*, Springer.; Graduate Texts in Physics; Berlin, Heidelberg, 2010.

(39) Vogl, P.; Hjalmarson, H. P.; Dow, J. D. A Semi-Empirical Tight-Binding Theory of the Electronic Structure of Semiconductors. *J. Phys. Chem. Solids* **1983**, *44*, 365–378.

(40) Yamada, Y.; Nakamura, T.; Endo, M.; Wakamiya, A.; Kanemitsu, Y. Near-Band-Edge Optical Responses of Solution-Processed Organic–inorganic Hybrid Perovskite $CH_3NH_3PbI_3$ on Mesoporous TiO_2 Electrodes. *Appl. Phys. Express* **2014**, *7*, 32302.

(41) Miyata, A.; Mitioglu, A.; Plochocka, P.; Portugall, O.; Wang, J. T.-W.; Stranks, S. D.; Snaith, H. J.; Nicholas, R. J. Direct Measurement of the Exciton Binding Energy and Effective Masses for Charge Carriers in Organic-Inorganic Tri-Halide Perovskites. *Nat. Phys.* **2015**, *11*, 582–587.

(42) Lindblad, R.; Bi, D.; Park, B.; Oscarsson, J.; Gorgoi, M.; Siegbahn, H.; Odelius, M.; Johansson, E. M. J.; Rensmo, H. Electronic Structure of TiO2 /CH3NH3PbI3 Perovskite Solar Cell Interfaces. *J. Phys. Chem. Lett.* **2014**, *5*, 648–653.

(43) Endres, J.; Egger, D. A.; Kulbak, M.; Kerner, R. A.; Zhao, L.; Silver, S. H.; Hodes, G.; Rand, B. P.; Cahen, D.; Kronik, L.; et al. Valence and Conduction Band Densities of States of Metal Halide Perovskites: A Combined Experimental–Theoretical Study. *J. Phys. Chem. Lett.* **2016**, *7*, 2722–2729.

(44) Kong, L.; Liu, G.; Gong, J.; Hu, Q.; Schaller, R. D.; Dera, P.; Zhang, D.; Liu, Z.; Yang, W.; Zhu, K.; et al. Simultaneous Band-Gap Narrowing and Carrier-Lifetime Prolongation of Organic–inorganic Trihalide Perovskites. *Proc. Natl. Acad. Sci.* **2016**, *113*, 8910–8915.

(45) Jin, H.; Im, J.; Freeman, A. J. Topological Insulator Phase in Halide Perovskite Structures. *Phys. Rev. B* **2012**, *86*, 121102.

(46) Even, J.; Pedesseau, L.; Dupertuis, M. A.; Jancu, J. M.; Katan, C. Electronic Model for Self-Assembled Hybrid Organic/perovskite Semiconductors: Reverse Band Edge Electronic States Ordering and Spin-Orbit Coupling. *Phys. Rev. B* **2012**, *86*, 205301.

(47) Pedesseau, L.; Jancu, J.; Rolland, A.; Deleporte, E.; Katan, C.; Even, J.; Pedesseau, L.; Jancu, J.; Rolland, A.; Deleporte, E.; et al. Electronic Properties of 2D and 3D Hybrid Organic / Inorganic Perovskites for Optoelectronic and Photovoltaic Applications. *Opt. Quantum Electron.* **2014**, *46*, 1225–1232.

(48) Wood, D. R.; Ross, C. B.; Scholl, P. S.; Hoke, M. L. Interferometric Measurement of Pb Ii Spectrum. *J. Opt. Soc. Am.* **1974**, *64*, 1159–1161.

(49) Vergès, E. L.-K. and C. M. and J. Etude Expérimentale et Théorique de l'Iode Atomique. Observation Du Spectre d'Arc Infrarouge, Classification et Structure Hyperfine. *Phys. Scr.* **1975**, *12*, 199.

(50) Katan, C.; Pedesseau, L.; Kepenekian, M.; Rolland, A.; Even, J. Interplay of Spin–orbit Coupling and Lattice Distortion in Metal Substituted 3D Tri-Chloride Hybrid Perovskites. *J. Mater. Chem. A* **2015**, *3*, 9232–9240.

(51) De Wolf, S.; Holovsky, J.; Moon, S.; Löper, P.; Niesen, B.; Ledinsky, M.; Haug, F.; Yum, J.; Ballif, C. Organometallic Halide Perovskites: Sharp Optical Absorption Edge and Its Relation to Photovoltaic Performance. *J. Phys. Chem. Lett.* **2014**, *5*, 1035–1039.

(52) Leguy, A. M. A.; Azarhoosh, P.; Alonso, M. I.; Campoy-Quiles, M.; Weber, O. J.; Yao, J.; Bryant, D.; Weller, M. T.; Nelson, J.; Walsh, A.; et al. Experimental and Theoretical Optical Properties of Methylammonium Lead Halide Perovskites. *Nanoscale* **2016**, *8*, 6317–6327.

(53) Even, J.; Carignano, M.; Katan, C. Molecular Disorder and Translation/rotation Coupling in the Plastic Crystal Phase of Hybrid Perovskites. *Nanoscale* **2016**, *8*, 6222–6236.

(54) Rakita, Y.; Cohen, S. R.; Kedem, N. K.; Hodes, G.; Cahen, D. Mechanical Properties of APbX 3 (A = Cs or CH_3NH_3; X = I or Br) Perovskite Single Crystals. *MRS Commun.* **2015**, *5*, 623–629.

(55) Jancu, J.-M.; Voisin, P. Tetragonal and Trigonal Deformations in Zinc-Blende Semiconductors: A Tight-Binding Point of View. *Phys. Rev. B* **2007**, *76*, 115202.